Energies **2013**, *6*, 2741-2758; doi:10.3390/en6062741

OPEN ACCESS

energies

ISSN 1996-1073

www.mdpi.com/journal/energies

Article

Turbulent Flow Characteristics and Dynamics Response of a Vertical-Axis Spiral Rotor

Can Kang [1,*], Xin Yang [1] and Yuli Wang [2]

[1] School of Energy and Power Engineering, Jiangsu University, Zhenjiang 212013, China; E-Mail: xinyangujs@gmail.com

[2] Department of Mechanics, KTH Royal Institute of Technology, Stockholm SE-100 44, Sweden; E-Mail: yuli@mech.kth.se

* Author to whom correspondence should be addressed; E-Mail: kangcan@mail.ujs.edu.cn; Tel.: +86-511-8878-0217; Fax: +86-511-8878-3105.

Received: 28 March 2013; in revised form: 15 May 2013 / Accepted: 17 May 2013 / Published: 29 May 2013

Abstract: The concept of a vertical-axis spiral wind rotor is proposed and implemented in the interest of adapting it to air flows from all directions and improving the rotor's performance. A comparative study is performed between the proposed rotor and conventional Savonius rotor. Turbulent flow features near the rotor blades are simulated with Spalart-Allmaras turbulence model. The torque coefficient of the proposed rotor is satisfactory in terms of its magnitude and variation through the rotational cycle. Along the height of the rotor, distinct spatial turbulent flow patterns vary with the upstream air velocity. Subsequent experiments involving a disk generator gives an in-depth understanding of the dynamic response of the proposed rotor under different operation conditions. The optimal tip-speed ratio of the spiral rotor is 0.4–0.5, as is shown in both simulation and experiment. Under normal and relative-motion flow conditions, and within the range of upstream air velocity from 1 to 12 m/s, the output voltage of the generator was monitored and statistically analyzed. It was found that normal air velocity fluctuations lead to a non-synchronous correspondence between upstream air velocity and output voltage. In contrast, the spiral rotor's performance when operating from the back of a moving truck was significantly different to its performance under the natural conditions.

Keywords: spiral wind rotor; numerical simulation; turbulent flow pattern; dynamic response; experiment

---

1. Introduction

The wind turbine is one of the most economically viable renewable energy conversion systems with the turbine's aerodynamic and structural performance having a direct impact on the performance of the whole system [1]. In recent years there have been significant developments in large capacity horizontal-axis wind turbine rotors and consistent improvements in the performance of vertical-axis wind turbines. The well-known Betz limit caps the maximum ratio of transformable wind energy by wind rotor, however significant effort is still being devoted to wind turbine innovation, especially for vertical-axis wind turbines. The Savonius rotor has been continuously investigated since 1924. The geometrical profile of the rotor has evolved from the original cylindrical type to twisted, spiral and other types. Conventional drag machine has been substantially renovated to include a combination of lift and drag characteristics. In spite of the low energy transformation efficiency of conventional Savonius rotor, its high start-up torque and simple mechanical structure are two significant advantageous factors that suggest a promising future for this kind of rotor. A recent review of Savonius wind turbine by Fan *et al.* [2] summarizes its advantages and applications.

Several researchers have implemented new ideas for improving the performance of conventional Savonius rotors. Fan *et al.* [3] designed a twisted Savonius rotor blade and the geometry was proved to be feasible for low-air-velocity conditions. Gupta *et al.* [4] studied a combined Savonius–Darrieus type rotor. In their work, a three-bucket Savonius rotor was placed on top of a three-blade Darrieus rotor; the combined rotor had an efficiency of 51% under a non-overlapping flow condition. With a front guide-box tunnel, Kunio *et al.* [5] attempted to make Savonius rotor adapt to different air velocities. Burcin *et al.* [6,7] designed a curtain arrangement and placed it in front of a Savonius rotor to prevent the production of negative torque and accelerate the air flow approaching the rotor. It was shown that the rotor with a curtain exhibits better performance than the rotor without a curtain. Menet [8] built a small double-step Savonius rotor prototype and tested the rotor with a rewound conventional car alternator. A similar concept was also discussed and experimentally studied by Mahmoud [9]. Sometimes it is feasible to install a deflector before the wind rotor, which contributes to an energy saving. The effect of the deflector is to change the flow field near the wind rotor and therefore the response of the rotor to the air flow [10]. In another study of a combined Savonius rotor, the overlap ratio and the phase shift angle were shown to be two critical parameters that influence the power output at different upstream air velocities [11].

The wind tunnel is important for evaluating the aerodynamic performance of wind rotors. Since a wind tunnel can provide steady and low turbulence upstream flow of adjustable magnitude, the turbine's characteristic parameters such as static torque, rotational speed and output power can be accurately measured. Saha *et al.* [12] tested a twisted blade in a low-speed wind tunnel and compared the performance data with that of a semicircular rotor blade. Li *et al*. [13] studied the conventional Savonius rotor without a central shaft in a wind tunnel. Kamoji *et al.* [14,15] studied a Savonius rotor with and without a central shaft in a wind tunnel and found that both the shaft and other geometrical parameters had remarkable effects on rotor's performance. Saha *et al.* [16] tested and analyzed the aerodynamic performance of single-stage, two-stage and three-stage Savonius rotors in a wind tunnel.

A rotor's performance depends essentially on the distribution of flow parameters and flow patterns around it. Fulisawa *et al.* [17] observed the flow field around a Savonius rotor utilizing a laser light

sheet and a CCD camera at a shutter speed of 0.002 s. This work showed that regions of flow separation on the blade surfaces were reduced due to the rotational effect. Flow through the overlap is weakened by the resisting flow. Both the torque and the flow phenomena are highly relevant to the transformation of wind energy. With particle image velocimetry (PIV) technology, Nobuyuki [18] measured the flow fields in and around a Savonius rotor at different overlap ratios. They showed that the overlap ratio affects both the flow passing through the overlap and the intensity of the downstream vortices.

Computational Fluid Dynamics (CFD) is an effective tool to predict a wind turbine's rotor performance. Some complicated flow phenomena can also be numerically visualized using CFD [19]. The idea of improving Savonius rotor's performance through optimization of the geometrical structure of the rotor can be effectively undertaken using CFD [20]. With numerical simulation, even the sophisticated problem of modeling the wake flow downstream of a wind farm can be reasonably solved with highly adaptable models such as an actuator disc model [21]. However, whether simulation results are able to fully reflect the physical essence of turbulent flow remains to be investigated [22].

The dynamic response indicates the variation of operation parameters of a wind rotor with air flow parameters. As such the dynamic response is fundamentally transient and is bound up with both the rotor and the flow. The transient aerodynamic force imposed on the rotor is an immediate parameter to represent the dynamic response. Placide *et al.* [23] studied the transient forces by numerically solving the unsteady Reynolds-averaged Navier-Stokes (RANS) equations. However, there were perceivable uncertainties in the numerical simulation involving the interaction between fluid and solid.

Most studies on vertical-axis wind rotor were undertaken using both wind tunnel and CFD techniques, which is necessary but not sufficient in the development of a new wind rotor. In this study, a new design of spiral rotor is proposed. A comparative study between the new spiral rotor and conventional Savonius rotor is conducted. Using CFD, the three-dimensional turbulent flow patterns near the rotor are depicted. Torque coefficient determined from the aerodynamic forces acted on the blades is utilized to evaluate the energy transformation ability of the two rotors. Based on the CFD predictions, the operational performance of the spiral rotor is experimentally studied under natural flow conditions and relative-motion conditions which are produced with the turbine mounted to the back of a moving pickup truck. The variation of tip-speed ratio with air velocity is experimentally obtained. The dynamic response of the spiral rotor to air flow is reflected by transient voltage output with a disk generator. The relationship between air velocity and output voltage is analyzed statistically. Flow parameters and operation performance are expected to jointly account for the characteristics of the presented rotor.

2. Geometry of Proposed Spiral Rotor

The concept discussed in this study comes from conventional S-type vertical-axis Savonius rotor shown in Figure 1a. This rotor's good performance irrespective of the air direction is one of the main factors that motivate the development of the new rotor design. The new spiral rotor has two blades evenly distributed around the vertical axis. The three-dimensional geometrical model of each blade can be approximately created by sweeping a base profile (shown in Figure 1c) along a spirally ascending curve, as shown in Figure 1b. The performance of the new spiral rotor and conventional Savonius are

compared in this study. The two rotors are uniform in terms of the rotor height and rotor diameter. The spiral rotor is designed with the height H of 1.8 m, the aspect ratio H/D of 1.6, the overlap ratio a/D of 0.18, and the gap ratio e/D of 0.16. Along the rotor height, the spiral angle is 180°. It can be anticipated from the two geometric models that the flow patterns induced will be significantly different, even with identical upstream boundary condition.

Figure 1. (**a**) Savonius rotor; (**b**) Spiral rotor; (**c**) Base profile.

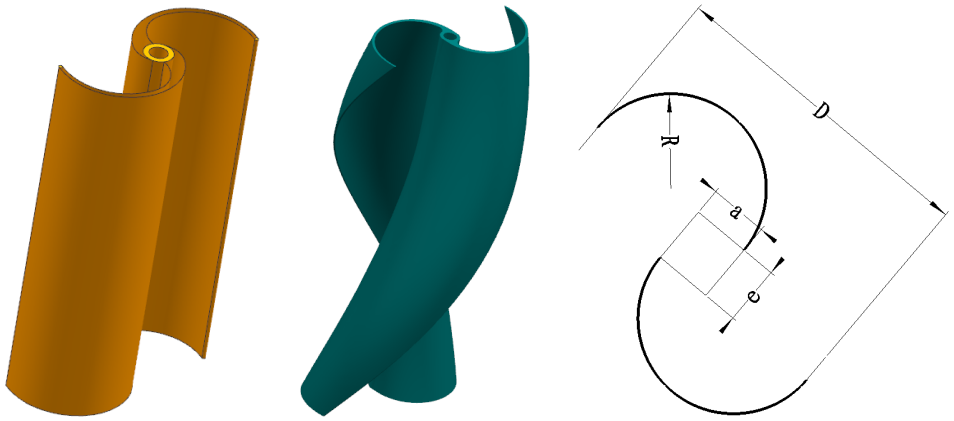

(**a**) (**b**) (**c**)

3. Numerical Simulation of the Flow around the Studied Rotors

CFD was used to evaluate the performance of the presented spiral rotor and to numerically predict the complicated three-dimensional turbulent flow patterns around the rotor. Commercial ANSYS-Fluent CFD code was used to undertake this analysis. A cuboid computational zone enclosing the rotor is discretized with a mesh consisting of 2,276,328 structured and unstructured elements. The dimensions of the computation zone are 15D along *x* direction (main flow direction), 2.6D along *y* direction (rotor-axis direction) and 5D along *z* direction (traverse direction). As a prerequisite, grid independence and verification of those empirical coefficients in the governing equations was undertaken in this study.

3.1. Turbulence Model

The flow field was set to be three-dimensional, viscous and incompressible. The one-equation Spalart-Allmaras turbulence model was applied to depict the turbulent viscosity transport. This turbulence model caters for flows involving adverse pressure gradient. The variables to be solved relate to highly turbulent viscosity. In the near-wall regions, the variable is linearly distributed along the vertical distance from the wall surface. As such the model is especially feasible when the mesh resolution is not sufficiently fine. The SIMPLEC algorithm was used to discrete the governing equations applied in the computation zone.

3.2. Boundary Conditions

The horizontal distance between the rotor's axis and the downstream outlet section is 10D, which meets the requirement of the full development of the wake flow downstream of the rotor. The vertical

wind shear effect at the inlet was ignored according to the practical operation conditions of the studied rotor. At the inlet of the computational zone, uniform velocity distribution was set and the velocity magnitude of 12 m/s was used in accordance with the rated design parameters. All outlet sections were set to be pressure outlets where local atmospheric pressure condition prevailed. Wall roughness was defined for all solid walls and a non-slip boundary condition was set at all solid walls. The interaction between rotating and non-rotating zones was treated utilizing the specific technique of moving mesh.

3.3. Performance and Discussion

3.3.1. Periodic Torque

Torque is one of the key parameters that directly influence the ability of energy transformation of a wind rotor [24]. Torque coefficient C_s is defined as:

$$C_S = \frac{4M}{\rho SDv^2} \tag{1}$$

where M is the torque acting on rotor shaft; ρ denotes air density; S is the upwind area of the rotor; and v denotes upstream air velocity.

For the two rotors with identical rotor height and rotor diameter, the variation of predicted torque coefficient with blade phase angle for an upstream air velocity of 12 m/s is shown in Figure 2.

Figure 2. Comparison of torque coefficients.

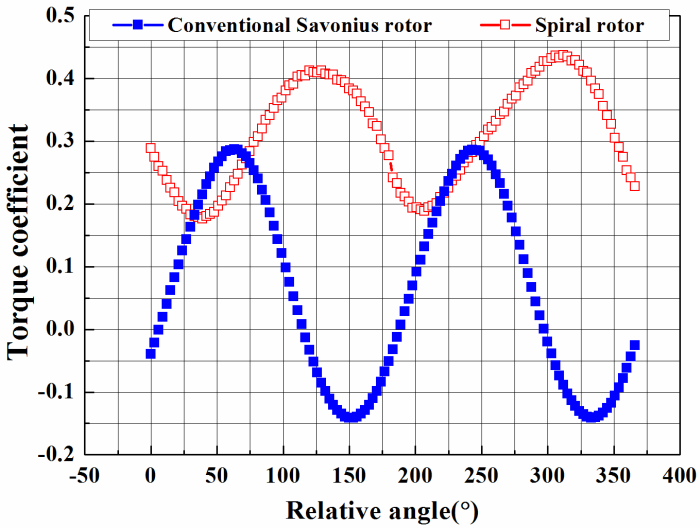

Here the rotational speed, ω, was set to 120 rpm and was defined during the computations, therefore the tip-speed ratio was the same for the two rotors. With respect to the geometrical profile of the spiral rotor and the conventional Savonius rotor, it is difficult to compare their torque performance based on the blade rotation angle. This angle denotes the relative position between upstream air flow and rotor's base section. For the conventional Savonius rotor, the angle does not vary along the rotor axis, which is different from that of the spiral rotor. Two torque coefficient curves corresponding to the blade rotation angle ranging from 0° to 360° are extracted from the simulation results after the residual errors converge to the limiting values. For the spiral rotor, the torque coefficient remains positive in the

whole rotational cycle and the difference between the maximum and minimum torque coefficients is nearly 0.21. The maximum torque coefficient is approximately 0.43. The corresponding maximum torque coefficient of the conventional Savonius rotor is lower than 0.30 and the fluctuation of torque coefficient is more severe. In particular a negative torque coefficient was found within two narrow ranges of blade rotation angle, which exactly reflects the intermittent disturbance to the flow field by the rotating blades with a uniform vertical profile. For the two rotors, similar periodic variation of torque coefficient is shown with respect to blade rotation angle.

3.3.2. Maximum Torque Coefficient

The maximum torque coefficient is connected to the rotor's performance and stable operation. For a range of upstream air velocity between 4 and 22 m/s, simulations were carried out when the spiral rotor was fixed at the relative angle at which the maximum torque coefficient was obtained. Similar treatment was applied to the conventional Savonius rotor. The results are displayed in Figure 3.

Figure 3. Variation of maximum torque coefficient with air velocity.

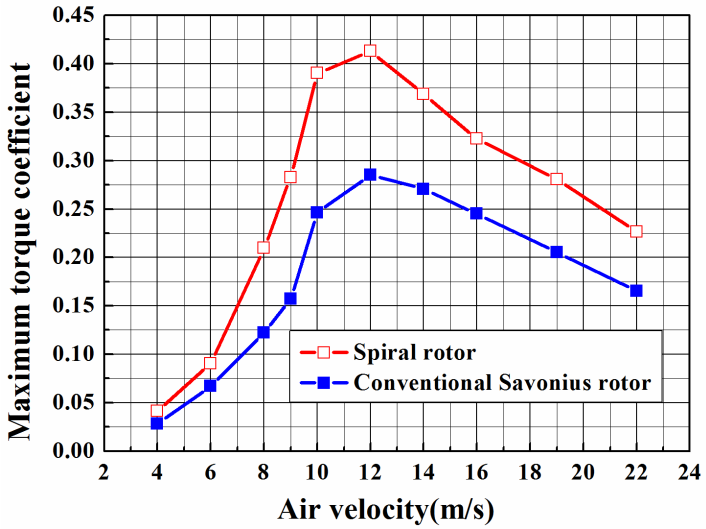

For the range of air velocities considered, the maximum torque coefficient appears at the blade rotation angle shown in Figure 2. As can be seen in Figure 3, the change in torque coefficient with respect to air velocity for both rotors is similar. The largest maximum torque coefficient appears when air velocity approaches the rated value. The maximum torque coefficient of the spiral rotor is consistently larger than its counterpart. For the spiral rotor, the optimal tip-speed ratio is very close to 0.48 which was guaranteed through the design. However, practical operating conditions will inevitably result in the deviation of tip-speed ratio from 0.48, which could lead to relatively poor and unstable torque performance.

The influence of rotor's rotational speed on torque performance is evident from Figure 3. However, the practical corresponding relationship between rotor rotational speed and air velocity can only be obtained through experimentation. Subsequently, the transient variation of torque with the blade rotation angle cannot be obtained using CFD.

3.4. Flow Parameters around the Rotor at Maximum Torque Coefficient

Sections through the blade at 0.5 H (Section B), 0.75 H (Section M) and 0.95 H (Section T) and vertical to the rotor axis were extracted from the computational results to display the three-dimensional turbulent features around the spiral rotor. Air flow is from left to right in Figures 4 and 5. For the conventional Savonius rotor, due to its uniform geometry along the rotor axis, the flow fields at each horizontal section are identical. Therefore, the flow field around conventional Savonius rotor is not presented here.

Figure 4. (**a**) Section B; (**b**) Section M; (**c**) Section T.

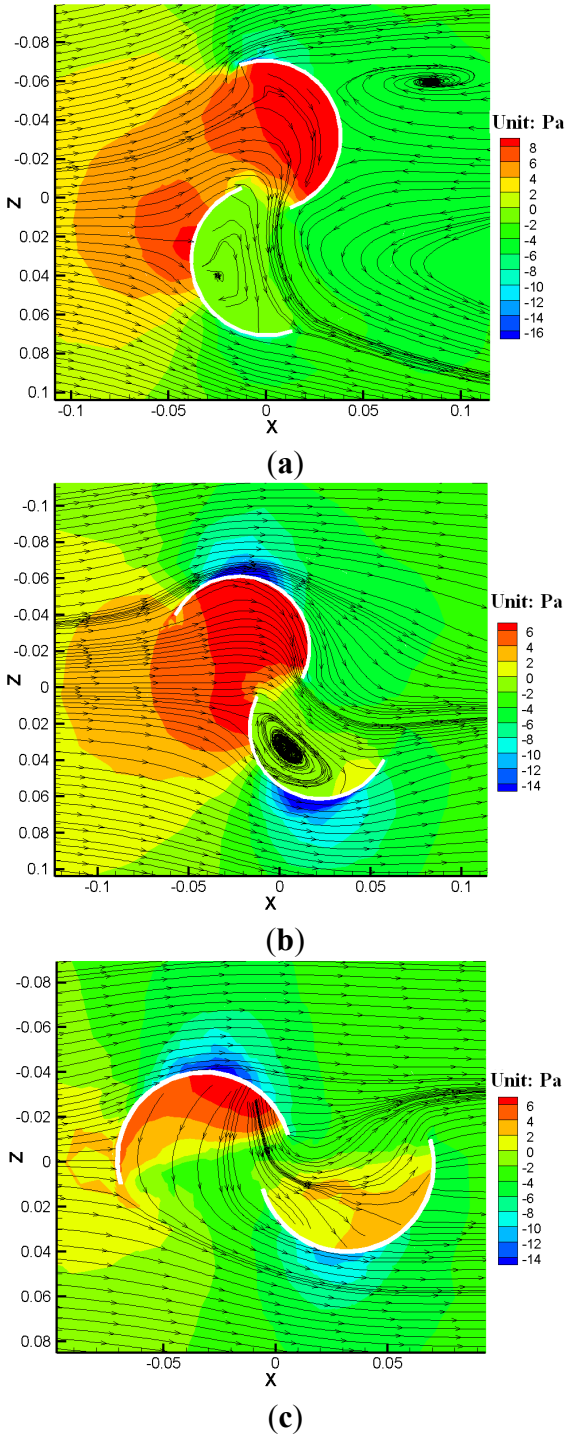

Figure 5. (**a**) Section B; (**b**) Section M; (**c**) Section T.

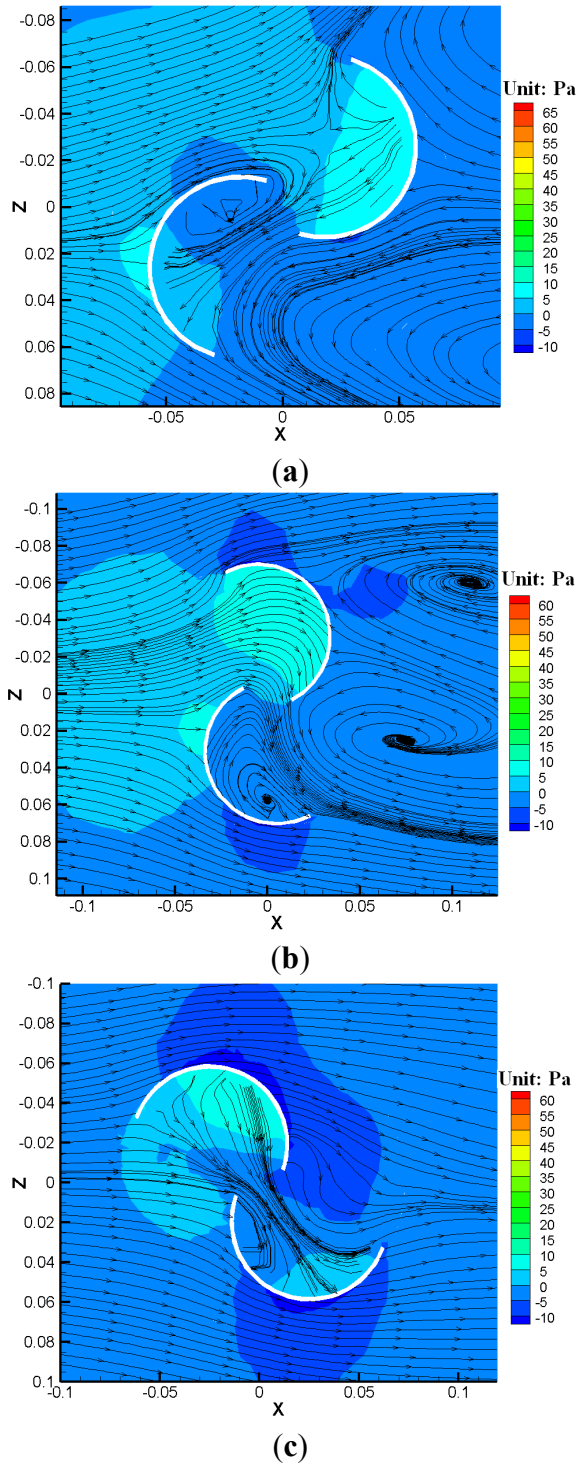

At the rated air velocity of 12 m/s, the pressure distributions and flow patterns at the maximum torque coefficient are shown in Figure 4 for the spiral rotor. The smoothest flow pattern is found at Section M where the pressure distribution contributes significantly to the creation of clockwise torque. The flow at Section B is expected to be similar to the flow around the conventional Savonius rotor for a pure-drag type rotor operating at the maximum torque coefficient. The rightward flow is resisted by the concave side of the upper blade. The pressure difference between the concave and convex sides of the upper blade results in the generation of clockwise torque which is simultaneously resisted by the

interaction between upstream air and the lower blade. The upstream air near the concave side of the lower blade is separated into two branches. One branch merges into the main stream after passing through the lower part of the lower blade, with the other passing through the gap between the two blades and enters the wake vortex zone along the diameter of the lower blade. Thereby a large-scale vortex appears near the concave side of the lower blade. Local resistance loss is remarkable at Section B.

At Section M, high-pressure zones near the concave side of the upper blade cover a large area and a low-pressure zone near the blade's convex side approaches the blade outer edge. Consequently, the large pressure difference at the blade outer edge gives impetus to the blade's clockwise rotation. Additionally, at the outer edge of the lower blade, the high-pressure zone at the concave side contributes to the production of clockwise torque as well.

In Figure 4c, the motion of the upstream air near the suction side of the left blade deviates from the direction of the main stream due to the blocking effect of the blade. The flow is divided into two branches. One branch joins the main stream and the other is separated into two sub-branches as it flows towards the right blade. Between the two sub-branches, one branch of the flow enters into the region near the suction side of the right blade and boosts the production of clockwise torque. The other branch is entrained by the flow passing through the gap between the two blades and joins the downstream wake zone.

3.5. Flow Parameters around the Rotor at Minimum Torque Coefficient

In order to further illustrate the formation of the torque on the rotor axis and correlate it with turbulent flow pattern, the flow field at the minimum torque coefficient is also obtained at certain blade rotation angles. The simulation was carried out with the same upstream boundary conditions.

The pressure distributions and flow patterns at minimum torque coefficient are displayed in Figure 5. For Section B and Section M, the pressure difference between the two sides of the upper blade is partly counteracted by the adverse pressure difference between the two sides of the lower blade. Two large-scale wake vortices with opposite rotating direction are found at Section M, which is similar to that shown in Figure 4a except that the core of the lower vortex is closer to the rotor and the vortex near the suction side of the lower blade is closer to the blade outer edge.

The flow at Section T has the greatest positive influence on the creation of clockwise torque. Distinct pressure difference exists between the two sides of the upper blade. After being accelerated, the flow branch passing through the gap between the two blades directly impinges the outer edge of the lower blade. A change of flow direction leads to the formation of local low-pressure zones at the pressure side of the lower blade. Moreover, the pressure difference between the two sides of the lower blade is remarkable.

In comparison to the results shown in Figure 4, the overall pressure difference is lower and more irregular for those shown in Figure 5. In Figure 5b,c, local high-pressure areas appear at the convex side of the blade, which will hinder the increase of positive static torque. It can also be deduced from Figures 4 and 5 that the creation of torque is essentially determined by pressure difference, flow pattern and the location of the largest pressure-difference between surfaces.

3.6. Spatial Flow Pattern

For the purpose of correlating the turbulent parameters along the rotor axis, three lines on the three sections studied separately are defined for the blade closer to the upstream air at maximum torque coefficient. As shown in Figure 6, upstream air flows along the positive *x*-direction and three lines coincide with the three diameter lines on the three blade sections, respectively. The velocity distribution on each line is displayed in Figure 7 in which the abscissa is expressed by dimensionless length ratio on the studied lines. The ratio of L/R = 0.0 corresponds to the point located at blade outer edge.

Figure 6. Top view of single blade along the rotor axis.

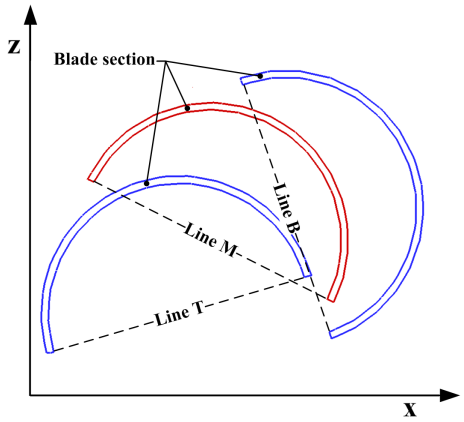

Figure 7. Spatial distribution of air velocity.

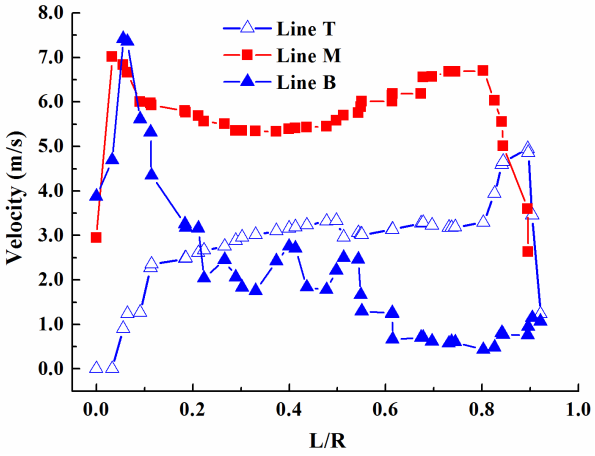

In Figure 7, from Line B to Line T, the overall inclination of velocity distribution curve relative to the horizontal axis changes from a downward state to an upward state and is bridged by relatively smooth velocity distribution at Line M. The maximum velocity magnitude appears near the blade outer edge at Line B and then the velocity decreases along Line B with increasing distance from blade outer edge. There are two evident peaks of velocity magnitude along line M. For Line T, the minimum velocity magnitude occurs near the blade's outer edge, while the peak value appears near the other end of Line T where the air passing through the gap is accelerating. It is verified here that distinct three-dimensional flow pattern is caused by the highly curved blade profile even if the rotor is fixed.

Along the rotor axis, the pressure difference between the two sides of each blade is distributed unevenly. During the rotor's rotation, an even more complicated distribution of pressure difference can result in the energy contained in the flow transformed into useful energy and various energy losses.

4. Experimental Set-Up

By undertaking the numerical simulation, we now have an understanding of both the spiral rotor's performance and the turbulent flow around the spiral rotor. In practical operation, assumptions such as the uniformity of the upstream air flow and stable rotation of the rotor will be rarely experienced. Additionally, the relationship between upstream air velocity and rotor's rotational speed cannot be predicted using CFD. Consequently, a full understanding of the spiral rotor cannot be accomplished using only CFD analysis.

A spiral rotor with the same geometry parameters as that studied numerically was fabricated, as shown in Figure 8. A four-wheel drive pickup truck was used as the carrier for the performance tests. The whole system consisted of a support frame fixed onto the platform of the truck through four bolts. The relative air velocity was produced by driving the pickup truck. The incoming air velocity to the rotor was measured by a well-calibrated hot-wire anemometer and measurements were undertaken when the fluctuation of air velocity was lower than 5% of the average air velocity. For the anemometer used, the measurable velocity ranged from 0.1 to 50 m/s. In this experiment, the systematical error in the velocity measurement is less than 0.01 m/s including temperature compensation.

Figure 8. Tested vertical-axis spiral rotor.

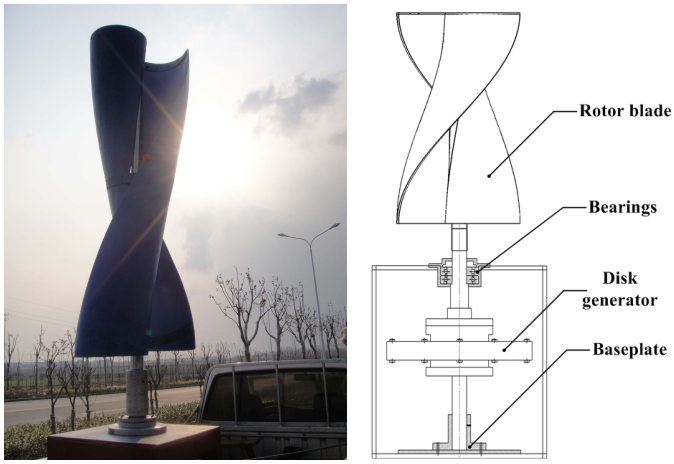

As shown in Figure 8, the shaft of the disk generator is fixed securely on the supporting frame. The disk generator is connected to the rotor via a shaft. The bearing housing is also fixed onto the baseplate. The vertical distance between the top of the cab and the bed of the cabin is 0.93 m. With the height of the frame supporting the wind rotor being considered, the bottom edge of the rotor blade was about 80 mm lower than the top of the cab. Furthermore, the wind rotor and its base were placed in the rear part of the carriage and the horizontal distance between the rotor axis and the back wall of the cab was 1.49 m. With the rotor shaft prevented from rotating via a brake, the truck speed was increased from 0 to 12 m/s, we found that the difference between the measured average velocities of the approaching flow at the bottom, middle and top parts of the rotor was less than 5%. So the influence of

the wake flow from the cab was considered to have a negligible effect on the flow experienced by the rotor.

During the experimental period and with the truck stationary, the natural wind velocity was less than 10 m/s. Experiments undertaken with the truck moving occurred when the natural wind velocity was less than 0.7 m/s, so the influence of natural wind velocity was ignored.

As shown in Figure 8, a disk generator is directly driven by the wind rotor. A circuit involving light bulbs of different powers served as the adjustable electrical load. The output voltage was measured with a multi-meter. A digital high precision revolution measurement instrument was used to measure the rotational speed of the rotor shaft.

With the experiment setup, air velocity, rotational speed of the rotor and the output voltage of the disk generator were obtained. As mentioned above, the air velocity and corresponding rotational speed of the rotor are two important factors to determine the tip-speed ratio. Output voltage is deemed as the characteristic parameter to illustrate the dynamic response of the rotor to air flow. In the experiment, data were acquired over a 2 min time interval and then statistically analyzed.

5. Experimental Results and Discussion

5.1. Test of Disk Generator

The disk generator used in the experiment was tested in the laboratory according to relative test standard before the on-site experiment. The variation of power output within the rotational speed range between 150 and 300 rpm is plotted in Figure 9. It can be judged from the steadily increased power output with rotational speed that the generator is sufficiently sized to be used in the experiments.

Figure 9. Performance of the disk generator.

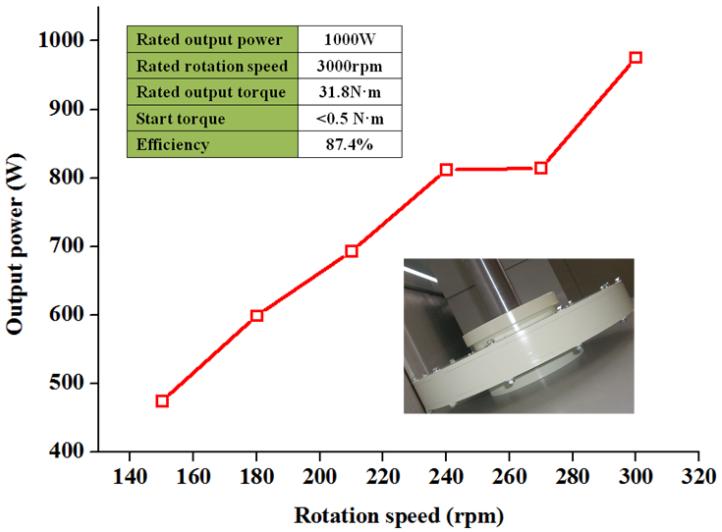

5.2. Results under Natural Conditions

Most wind turbines operate under natural conditions. Due to blockage effects and the artificial uniform nature of the upstream air flow, the results obtained during wind tunnel tests often do not coincide with the rotor's on-site operation. In the experiment with the pickup truck being kept

motionless, sampling was conducted under natural air flow conditions. All detected air velocities were less than 10 m/s. Three typical conditions were selected in the sampling data to provide evidence of the rotor's dynamic response to local ambient air flow. The results are displayed in Figure 10. In terms of relative velocity fluctuations, a distinct difference was found between the results in Figure 10 and the usual results obtained in a wind tunnel. Variation of the aerodynamic loads imposed on the wind rotor can be reasonably predicted. The area of the blade surface facing the upstream varies with rotor rotation, so the force on the surface of the rotor blades and the torque on the shaft consequently change.

Figure 10. Variation of air velocity under natural conditions.

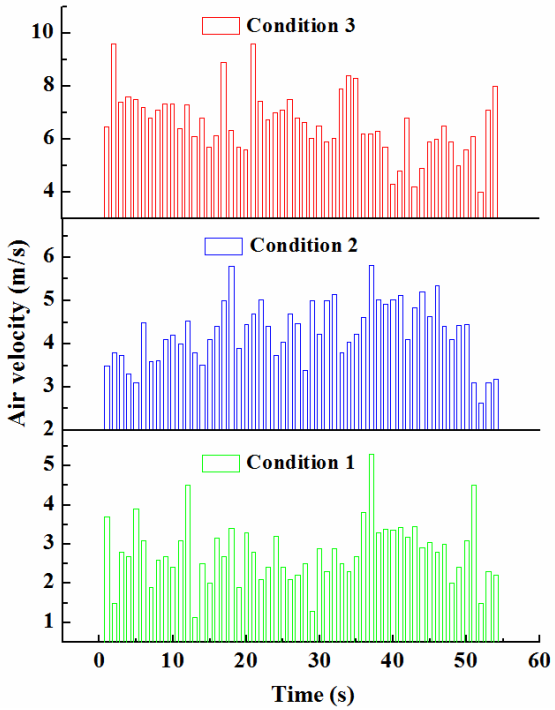

Under the three natural conditions 1, 2 and 3 denoted in Figure 10, statistically obtained time-averaged air velocities are 2.88 m/s, 4.8 m/s and 6.51 m/s, respectively. Corresponding output voltages are 24.1 V, 47.8 V and 106 V, respectively.

Variation of output voltage under the three conditions in Figure 10 is shown in Figure 11. For Condition 1, when the air velocity varies within the range of 1.0 to 5.6 m/s, the voltage changes within the range of 0 to 65 V. In practical applications, if the disk generator operates at an air velocity of less than 6 m/s, a method to increase and rectify the voltage should be adopted. The results show the variation in transient air velocity and the generator output voltage is not synchronous, so a comprehensive study of variation of air velocity, inertia of rotor blades and the subsequent response of disk generator is necessary. One of the disk generator's properties lies in the non-accordance between the output voltage and transient air velocity. The peak values in voltage are directly related to the velocity fluctuations.

For Condition 2, the air velocity smoothly changes with time. However, the overall magnitude of air velocity is large and the time-averaged air velocity reaches 4.28 m/s. The averaged output voltage is 47.8 V, which indicates that the positive effect of high air velocity on output voltage.

The maximum air velocity is found in Condition 3 with a time-averaged air velocity of 6.51 m/s. The corresponding averaged voltage output is 106 V. The response lag of voltage to air flow is mitigated with the increase of air velocity. In addition, voltage fluctuations are mitigated with the increase of air velocity as well.

Figure 11. Output voltage under natural conditions.

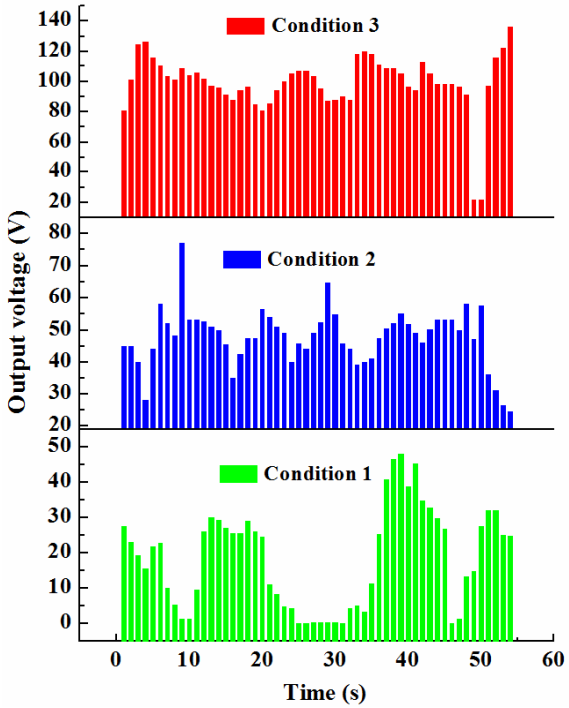

5.3. Variation of Tip-Speed Ratio

With the blade phase angle being adjusted to the angle corresponding to the maximum static torque coefficient, a test was carried out when the truck's travelling speed increases gradually. It was found that the rotor started to rotate at an air velocity of 1.95 m/s, which illustrates the good start-up ability of the spiral rotor.

A wind rotor's aerodynamic behavior can be highly affected by tip-speed ratio. However, tip-speed ratio is difficult to be accurately pre-defined during any numerical simulation. With experimental results, we can measure the air velocity and rotor's rotational speed and therefore determine its tip speed ratio; the rotors tip-speed ratio as a function of air velocity for a velocity range of 2 to 12 m/s is displayed in Figure 12. With an increase in air velocity, the tip-speed ratio increases overall and becomes near constant within the air velocity range of 6 to 12 m/s. Tip-speed ratio of 0.47 is reached when the air velocity approaches 12 m/s. During the experiment, the energy losses owing to several factors such as mechanical friction and flow losses lead to a slower rotation of the rotor than in the numerical simulation.

In the simulation, the largest torque coefficient occurs at the air velocity of 12 m/s, which corresponds to the maximum tip-speed ratio in the experiment. The spiral rotor's optimal tip-speed ratio is 0.4–0.5 which is smaller than that of a conventional Savonius rotor. With a spiral profile, the

rotor is no more a pure-drag type rotor. The connection between air velocity, the rotor's rotational speed and the blade's geometrical parameters deserves more comprehensive experiments.

Figure 12. Variation of tip-speed ratio with air velocity.

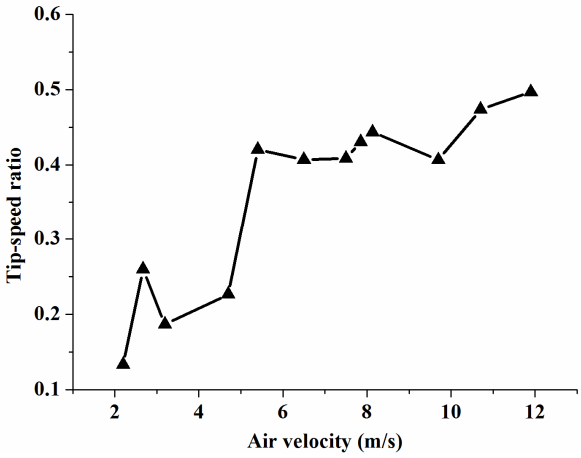

When the air velocity is low and fluctuating, the inner axial air gap between the rotor and stator of the generator may lead to unbalance which could cause more resistance to the rotation of the generator's rotor. It is the combination of the unbalance, the inertia of the rotor and the fluctuating driving force that decides the fluctuations of the tip-speed ratio at low air velocities. In the on-site experiment, both the rotational speed fluctuations and the mounting manner are different from that in the laboratory where the data in Figure 9 were obtained.

5.4. Results under Relative-Motion Conditions

As previously stated, experiments were undertaken with the truck moving when the local air velocity was less than 0.7 m/s. The pickup truck travelled almost orthogonal to the natural air flow to reduce the influence of local air velocity.

The experimental results under the two relative-motion conditions are displayed in Figure 13. Under Conditions 4 and 5, time-averaged air velocities are 10.5 and 7.64 m/s, respectively. The overall fluctuations under relative-motion conditions are much smaller than that under natural conditions. In Conditions 4 and 5, the air velocity fluctuations under Condition 5 are more evident. The difference between the results involving the pickup truck and that in wind tunnel is remarkable, illustrating the difficulty to implement an on-site wind turbine test. The corresponding variation of voltage output is shown in Figure 14. Under Condition 4, the time-averaged voltage reaches 192.1 V which is larger than 126.2 V obtained under Condition 5. In terms of the correspondence between voltage and transient air velocity, a more apparent relationship is found in Condition 4, showing that high air velocity and small fluctuation of air velocity are beneficial to the generator's response to the variation of air velocity.

Figure 13. Variation of air velocity under relative-motion conditions.

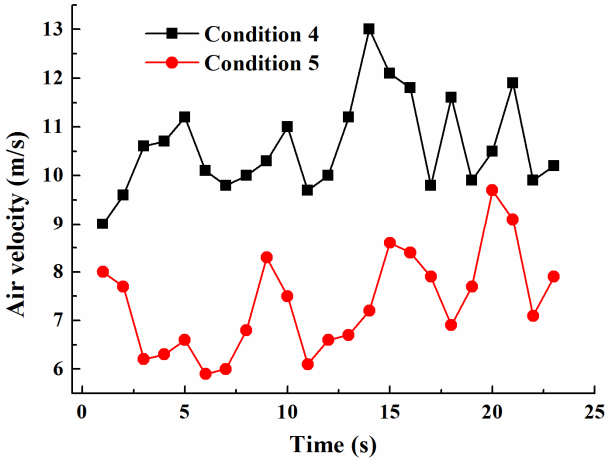

Figure 14. Voltage output under relative-motion conditions.

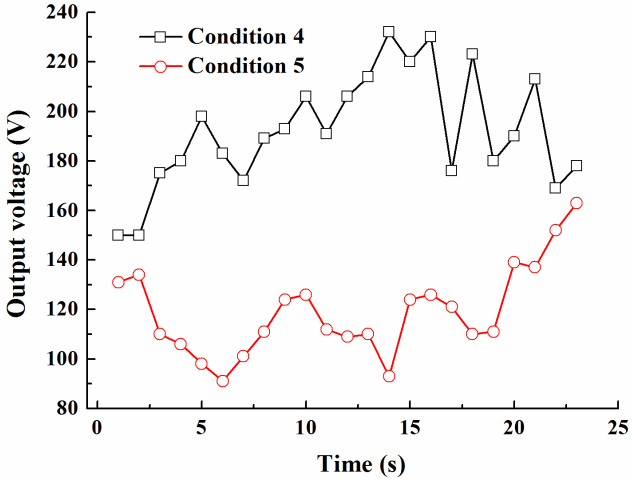

6. Conclusions

Turbulent features near the presented spiral rotor blade are studied through numerical simulation. The performance and dynamic response of a fabricated rotor are tested under natural and relative-motion conditions. Further investigations using the spiral rotor lies primarily in both the non-intrusive measurement of the velocity distribution near the rotor blades and the modulating of upstream turbulent parameters in the wind tunnel. The conclusions that can be drawn from this study are as follows:

(1) The turbulent flow field around the spiral rotor exhibits full three-dimensional features. The aerodynamic factors contributing to the creation of torque can be qualitatively elucidated by the distribution of static pressure. The torque performance of the spiral rotor is satisfactory in terms of the magnitude of the torque and the difference between the maximum and minimum torques;

(2) The optimal tip-speed ratio of the spiral rotor is 0.4–0.5, which is shown in both the numerical study and by experiment. The spiral rotor clearly does not belong to the category of pure-drag type wind rotor. An optimal tip-speed ratio is necessarily related to the flow around the rotor blades. Special effort should be devoted to decompose the aerodynamic force acting on the spiral surface.

(3) The experiments under both natural and relative-motion conditions were performed. Strong correlation between the generators output voltage and air velocity occurred under relative-motion conditions, the results under natural conditions reflect the actual operation of a wind rotor. Large and stable air velocity mitigates partially the transient variation of the loads on blade surface and enhances the effective driving force. However, the ideal conditions are not witnessed during the operation of most wind turbines.

Acknowledgments

This study is financially supported by the Priority Academic Program Development of Jiangsu Higher Education Institutions (PAPD), College Industrialization Project of Jiangsu Province (Grant No. JHB2011-37).

Conflict of Interest

The authors declare no conflict of interest.

References

1. Lin, Z.H. Wind energy and its utilization. *Chin. J. Nat.* **2009**, *30*, 309–314.
2. João, V.A.; Horácio, A.V.; Adriane, P.P. A review on the performance of Savonius wind turbines. *Renew. Sustain. Energy Rev.* **2012**, *16*, 3054–3064.
3. Fan, Z.P.; Wang, X.C.; Du, H.X.; Wang, Y.J. An innovative design of vertical-axis wind turbines for home use. *Energy Technol.* **2007**, *28*, 279–283.
4. Gupta, R.; Biswas, A.; Sharma, K.K. Comparative study of a three-bucket Savonius rotor with a combined three-bucket Savonius-three-bladed Darrieus rotor. *Renew. Energy* **2008**, *33*, 1974–1981.
5. Kunio, I.; Jitendro, N.R. Characteristics of wind power on Savonius rotor using a guide-box tunnel. *Exp. Therm. Fluid Sci.* **2007**, *32*, 580–586.
6. Burcin, D.A.; Mehmet, A. An experimental and numerical study on the improvement of the performance of Savonius wind rotor. *Energy Conv. Manag.* **2008**, *49*, 3425–3432.
7. Burcin, D.A.; Mehmet, A.; Özdamar, A. An experimental study on improvement of a Savonius rotor performance with curtaining. *Exp. Therm. Fluid Sci.* **2008**, *32*, 1673–1678.
8. Menet, J.L. A double-step Savonius rotor for local production of electricity: A design study. *Renew. Energy* **2004**, *29*, 1843–1862.
9. Mahmoud, N.H.; El-Haroun, A.A.; Wahba, E.; Nasef, M.H. An experimental study on improvement of Savonius rotor performance. *Alex. Eng. J.* **2012**, *51*, 19–25.
10. Daegyoum, K.; Morteza, G. Efficiency improvement of straight-bladed vertical-axis wind turbines with an upstream deflector. *J. Wind Eng. Ind. Aerodyn.* **2013**, *115*, 48–52.
11. Kumbernuss, J.; Chen, J.; Yang, H.X.; Lu, L. Investigation into the relationship of the overlap ratio and shift angle of double stage three bladed vertical axis wind turbine (VAWT). *J. Wind Eng. Ind. Aerodyn.* **2012**, *107–108*, 57–75.
12. Saha, U.K.; Rajkumar, M.J. On the performance analysis of Savonius rotor with twisted blades. *Renew. Energy* **2006**, *31*, 1776–1788.

13. Yan, L.; Hara, Y.; Hayashi, T. The performance effects of overlap ratio on Savonius rotor. *Renew. Energy Resour.* **2008**, *26*, 31–33.
14. Kamoji, M.A.; Kedare, S.B.; Prabhu, S.V. Experimental investigations on single stage modified Savonius rotor. *Appl. Energy* **2009**, *86*, 1064–1073.
15. Kamoji, M.A.; Kedare, S.B.; Prabhu, S.V. Performance tests on helical Savonius rotors. *Renew. Energy* **2009**, *34*, 521–529.
16. Saha, U.K.; Thotla, S.; Maity, D. Optimum design configuration of Savonius rotor through wind tunnel experiments. *J. Wind Eng. Ind. Aerodyn.* **2008**, *96*, 1359–1375.
17. Fujisawa, N.; Gotoh, F. Visualization study of the flow in and around a Savonius rotor. *Exp. Fluids* **1992**, *12*, 407–412.
18. Nobuyuki, F. Velocity measurements and numerical calculations of flow fields in and around Savonius rotors. *J. Wind Eng. Ind. Aerodyn.* **1996**, *59*, 39–50.
19. Ivan, D.; Fawaz, M. CFD and PIV investigation of unsteady flow through Savonius wind turbine. *Energy Procedia* **2011**, *6*, 711–720.
20. Mohamed, M.H.; Janiga, G.; Pap, E.; Thévenin, D. Optimal blade shape of a modified Savonius turbine using an obstacle shielding the returning blade. *Energy Convers. Manag.* **2011**, *52*, 236–242.
21. Francesco, C.; Andrea, V. An application of the actuator disc model for wind turbine wakes calculations. *Appl. Energy* **2013**, *101*, 432–440.
22. Zhou, T.; Dietmar, R. Numerical study of detailed flow field and performance of Savonius wind turbines. *Renew. Energy* **2013**, *51*, 373–381.
23. Placide, J.; Sean, M.T.; François, G.; Alain, B. An analysis of the transient forces acting on Savonius rotors with different aspect ratios. *Renew. Energy* **2013**, *55*, 286–295.
24. Fang, F.; Li, S.M.; Li, Y.; Xu, D. Torque characteristics simulation on small scale combined type vertical-axis wind turbine. *Phys. Procedia* **2012**, *24*, 781–786.